Water/oil nanoemulsion-based synthesis of $Bi_xSn_{6-2x}S_y$ ($0.33 \leq x \leq 2.95$) semiconductor QDs for efficient photocatalytic degradation of MB dye

Mosaad R Negem [a], David Miller [b], John Irvine [b], Fakiha El-Taib Heakal[c*]

[a]*Chemistry Department, Faculty of Science, Fayoum University, Fayoum-Egypt*
[b]*School of Chemistry, EaSTChem, University of St Andrews, St Andrews, Fife KY16 9ST, UK*
[c]*Chemistry Department, Faculty of Science, Cairo University, Giza 12613, Egypt*

Abstract

The development of efficient photocatalysts for the photodegradation of organic dyes in wastewater is highly worthwhile. Herein, the nanoemulsion tactic was utilized to synthesize $Bi_xSn_{6-2x}S_y$ ($0.33 \leq x \leq 2.95$) photocatalysts with morphological structures that changed from nanowhiskers to quantum dots (QDs). The optical properties of these materials were examined by UV-visible absorbance spectroscopy and photoluminescence, while Mott-Schottky analysis was utilized to study their electronic properties. $Bi_xSn_{6-2x}S_y$ materials exhibit appreciable absorption in the UV-visible light range with a direct band gap that increases from 1.23 to 1.46 eV. Both crystal structure and composition greatly affect the photocatalytic activity of $Bi_xSn_{6-2x}S_y$ semiconductors. Among the various synthesized photocatalysts, $BiSn_4S_{4.5}$ can efficiently photodegrade methylene blue dye (MB) in the shortest time under UV-visible light. The photocatalytic activity is positively affected by the change of crystal structure from orthorhombic to cubic symmetry. Based on the Mott-Schottky plots, the flat band potential (E_{fb}) and the semiconductor behavior of the fabricated $Bi_xSn_{6-2x}S_y$ nanomaterials were determined. The obtained E_{fb} values for SnS, $Bi_{0.33}Sn_{5.34}S_{5.8}$, $BiSn_4S_{5.5}$, and $Bi_{2.14}Sn_{1.71}S_{4.7}$ are -0.18 V, -0.42 V, -0.53 V, and -0.51 V (vs. Ag/AgCl), respectively. The E_{fb} value is clearly shifted towards more negative potential values with increasing the Bi molar ratio (x). However, $Bi_{2.95}Sn_{0.1}S_{4.5}$ semiconductor was found to be of n-type character, having a positive E_{fb} value of +0.66 V (vs. Ag/AgCl). Photocurrent responses confirm the high stability and photocatalytic activity of $BiSn_4S_{5.5}$, which also achieves the lowest charge transfer resistance. The modified

electronic properties of the $Bi_xSn_{6-2x}S_y$ semiconductors significantly improve their photocatalytic activity, rendering them to be promising absorbers for sunlight harvesting applications.

Keywords: Metals chalcogenides; Nanoemulsion tactic; Semiconductor quantum dots; Direct band gap; MB photodegradation; Mott-Schottky plots.

---

*Corresponding authors: E-mail address: hfakiha@cu.edu.eg (F.E. Heakal).

Introduction

Solar energy is known to be the most sustainable source of energy on our planet for being renewable, huge, and clean. Nanomaterials such as semiconductors (Xu et al. 2012), metals (Gupta et al. 2022), alloys (Nady and Negem 2016), and composites (Negem and Nady 2020) are useful for energy conversion. Semiconductors especially are materials having the ability to convert solar energy into chemical and electrical energy. The semiconductors absorb light across the band gap and convert it into electrical energy and photocatalyzed chemical reaction (Xu et al. 2012). The process occurs via three steps including light absorption, separation, and transport of photoproduced electrons and holes from bulk to the surface. This scenario has an influential role in the efficiency of the semiconductors to harvest sunlight energy (Liu and Chen 2014).

Nanomaterials display multiple morphological structures among them quantum dots (QDs) with a grain size range of 1-10 nm. Semiconductor QDs are those nanomaterials of dimensions smaller than the excitation radius of Bohr (an excitation is an electron/hole pair) (Huang and Zhu 2013). Furthermore, metals chalcogenides semiconductor QDs have great importance as they possess high molar absorptivity and broad absorption (Lim et al. 2011), tuneable optical properties (Nguyen et al. 2014), exceptional electronic properties (Cassette et al. 2010), as well as considerable intrinsic dipole moment (Mora-sero et al. 2009). Because of their exceptional properties, they have inclusive applications in photocatalysis since

they possess immense surface area among other types of nanomaterials. In addition, they can be exploited in optoelectric applications, sensors, and batteries' electrodes (Chao et al. 2012). These semiconductors show a band gap ranging between 0.9 eV and 1.9 eV and are appropriate absorbers for sunlight utilized in photovoltaic devices (Gerein and Haber 2006) and photocatalysis (Zhang et al. 2022). For that, they have been used in the photocatalytic degradation of organic pollutants such as azo dyes, which are actually released by several industries and seriously affect the environment and the ecosystems due to their toxic and carcinogenic nature. The photodegradation process can seamlessly decompose the organic dyes completely and effectively in a very short time.

Synthesis of semiconductors using abundant and inexpensive elements is crucial for wastewater treatment and other solar energy applications. Our designed $Bi_xSn_{6-2x}S_y$ materials are a good example characterized by low-cost and low toxicity compared to cadmium sulfide CdS), which makes them ideal materials to produce affordable photocatalysts. Likewise, SnS attracts great interest because of its widespread applications, for having a high absorption coefficient of sunlight, and tuneable band gap that varies between 1.1 eV to 1.6 eV (Li et al. 2015; Liu et al. 2014; Antunez et al. 2014; Li et al. 2015; Pankove 1971). In the meantime, Bi_2S_3 displays a low band gap ranging between 1.3 eV to 1.7 eV, which renders it to be considered an excellent harvester for sunlight in UV-visible and near-IR regions with an absorption coefficient of about 10^4 to 10^5 cm^{-1} and tuning light absorbance properties. $Bi_xSn_{6-2x}S_y$ nanomaterials are composed of earth-abundant non-toxic elements and can be used to synthesize photovoltaic devices depending on the low toxic substances (Bernechea et al. 2015). Nanomaterials are commonly synthesized using a variety of techniques, relying on key parameters such as cost, simplicity, material recycling, speed, and low power consumption. Indeed, nanoemulsion is thought to be the most appropriate technique for possession of all these indicators, and can therefore be used to manufacture nanomaterials, especially QDs.

The immiscibility of ionic liquid/water and hydrocarbon compounds/oil causes the formation of two phases during mixing because of the high value of interfacial tension force between water/oil (~ 0.03-0.05 N/m) (Gelbart and Ben-Shaul 1996). The addition of surfactants can easily overcome the interfacial tension force between water/oil and forms a single phase from the nanoemulsion. The reverse micelles are a well-organized collection of surfactants where the ionic head is attracted to water and the long-organic tail is attracted to the oil. The size of the reverse micelle changes from 2 to 50 nm (Sanchez-Dominguez et al. 2012) and can be used as nanoreactors, which encompass reactants and controlling the product size to produce homogenous nanomaterials. Based on this approach, the aim of the present innovative work was to synthesize $Bi_xSn_{6-2x}S_y$ ($0.33 \leq x \leq 2.95$) QDs photocatalyst and to enhance their efficiency by improving their ability to absorb solar light irradiation in the UV-visible region. The morphology characterization, optical properties, electronic behavior, and photocatalytic activity of the as-prepared nanomaterials were thoroughly investigated by various suitable techniques.

Experimental

Chemicals, Methods, Instruments, and Characterization

The chemicals 2-methyl pentane 99.9%, acetone, hydrochloric acid, and 1-propanol 99.9% were all bought from Fisher Scientific Company. Bi_2O_3 99%, $SnCl_2$ 99%, Na_2S 99.5% , Na_2SO_4 99.9%, methylene blue 99.9%, and sodium lauryl sulfate (SLS) 99.9% were purchased from Aldrich-Sigma. The composition of the nanoemulsion was 41.67% water, 41.67% oil phase (2-methyl pentane and 1-propanol), and 16.66% surfactant. Bi_2O_3 and $SnCl_2$ were dissolved in the water phase by adding a suitable amount of HCl as depicted in **Table 1**, which also includes the amounts of chemicals and solvents used. Similarly, in a separated nanoemulsion, S^{-2} ions were dissolved in the water phase and a similar amount of solvents were added to form a nanoemulsion of metal ions as shown in **Table 1**. All components of the

nanoemulsion were blended to form a single optically isotropic mixture under stirring at room temperature of 20 °C. Nanoemulsion of Bi^{3+} and Sn^{2+} ions were added to nanoemulsion of S^{-2} ions and stirred for 2 h to form nanostructured $Bi_xSn_{6-2x}S_y$. The nanostructured $Bi_xSn_{6-2x}S_y$ was separated and washed using a mixture of acetone or ethanol and water (2:3) and centrifuge, then dried under argon at room temperature, see **Fig. 1**.

Structural features of $Bi_xSn_{6-2x}S_y$ nanomaterials were measured using high-resolution transmission electron microscopy (HRTEM) and FEI SCIOS dual-beam. XRD patterns were obtained for $Bi_xSn_{6-2x}S_y$ using a Philips PW 1710 X-ray diffractometer operated in reflection mode. The XRD patterns of $Bi_xSn_{6-2x}S_y$ were analyzed with STOE WinXPOW software to determine the crystal structure and the unit cell parameters. The chemical composition of the $Bi_xSn_{6-2x}S_y$ was obtained using ionic inductively coupled plasma (ICP) spectroscopy and energy dispersive X-ray (EDX) analysis. UV-visible absorbance and band gap of the $Bi_xSn_{6-2x}S_y$ were obtained using the Jasco V-650 spectrometer in the wavelength range of 200 to 900 nm. Photoluminescence spectra were recorded using a JY Horiba Fluoromax 2 fluorimeter, with an excitation wavelength of 550 nm. The dried powders of nanostructure $Bi_xSn_{6-2x}S_y$ materials were then pressed into pellets (11 mm diameter and 4-6 mm thickness) using a pressure of 200 MPa, and silver wire was fitted using silver paste and dried at 70 °C for 10 min. Mott-Schottky plots were recorded over a step potential from -0.7 to 0.8 V (vs. Ag/AgCl) using Solartron SI 1255 instrument and the pressed pellet in a three-electrode cell system filled with 0.6 M Na_2SO_4 electrolyte. Photocurrent and EIS measurements were also recorded using a CHI 760E workstation at 0.65 V (vs. Ag/AgCl) under dark and UV-visible light. The working electrode was always the pressed pellet from each synthesized nanomaterial. All electrochemical tests were measured at least three times to achieve the repeatability of the measurements. Photocatalytic activity of the as-prepared nanostructure $Bi_xSn_{6-2x}S_y$ powder was carried out by observing the degradation of methylene blue (MB) dye under UV-visible light and visible light,

UV-visible light irradiation was produced by a 250 W iron-doped metal halide ultraviolet-visible lamp and visible light irradiation was obtained using an ultraviolet cut-off filter (λ > 420 nm; Borosilicate Coated Glass HM07, UQG (optic), Cambridge UK). For the photodegradation of MB (M. W. 320 g/mol), 20 mg $Bi_xSn_{6-2x}S_y$ powder was dispersed in a 100 mL aqueous solution of 1×10^{-4} M MB under stirring. The photocatalytic activity of the $Bi_xSn_{6-2x}S_y$ was then obtained using a Perkin Elmer Lambda 35 ultraviolet/visible spectrometer by monitoring the intensity of the strongest absorption peak of MB at 665 nm along with irradiation time. After that 2 mL of solution was withdrawn at various time intervals. The temperature during irradiation was stabilized at about 25 ºC by means of a water bath.

Results and Discussion

Nanostructure characterization of $Bi_xSn_{6-2x}S_y$

Figs. 2 and **3** show the HRTEM and SCIOS images for the as-prepared $Bi_xSn_{6-2x}S_y$ powders. The morphological structure of $Bi_{2.14}Sn_{1.71}S_{4.7}$, $BiSn_4S_{5.5}$, and $Bi_{0.3}Sn_{5.34}S_{5.8}$ is the uniform size of the QDs with spherical-like grains and size of about 2-5 nm as displayed in **Fig. 2**(b-e), which is confirmed by the broad peaks shown in the XRD pattern. Also, the QDs are single crystalline owing to the lattice fringes appearance (Niezgoda et al. 2012), while $Bi_{2.95}Sn_{0.1}S_{4.5}$ shows nanowhiskers structure as shown in Fig. 2(a) and **Fig. 3**(a, b). The formation of homogenous grains of QDs or nanowhiskers is due to identical micelles, which work as nanoreactors. The change in the morphological structure of $Bi_xSn_{6-2x}S_y$ from QDs to nanowhiskers can be attributable to a change in the pH of the nanoemulsion and replacing tin ions with bismuth ions having larger ionic sizes. This morphological structure would increase the photocatalytic activity, as the QDs structure possesses a huge surface area, which facilitates the accessibility of additional active binding sites on the adsorbent surface and thus accelerates charge transfer. ICP and EDX analyses showed that different compositions of $Bi_xSn_{6-2x}S_y$ were obtained such as SnS, $Bi_{0.3}Sn_{5.34}S_{5.8}$, $BiSn_4S_{5.5}$, $Bi_{2.14}Sn_{1.71}S_{4.7}$, and $Bi_{2.95}Sn_{0.1}S_{4.5}$ as depicted

in **Fig. 4**(a) and the inset of **Fig. 2**(b). The lowest value of the molar ratio (x) of Bi is 0.33 and the highest is 2.95 (**Table 1)**. **Fig. 4**(b) displays the digital images for the as-synthesized $Bi_xSn_{6-2x}S_y$ nanopowders, which change from brown to dark blue with increasing the Bi molar ratio (x) in the nanomaterials.

The XRD patterns of the as-prepared $Bi_xSn_{6-2x}S_y$ nanopowders are displayed in **Fig. 5**. All peaks are indexed with single-phase cubic-P unit cell for the compositions up to x = 2.14 molar ratio, including SnS, $Bi_{0.3}Sn_{5.34}S_{5.8}$, $BiSn_4S_{5.5}$, and $Bi_{2.14}Sn_{1.71}S_{4.7}$. The unit cell parameters of SnS, $Bi_{0.3}Sn_{5.34}S_{5.8}$, $BiSn_4S_{5.5}$, and $Bi_{2.14}Sn_{1.71}S_{4.7}$ were obtained and fitted using WinXPOW software. The unit cell of the cubic structure is consistent with a phase of In_2S_3 ICDD 01-084-1385 and the length of the unit cell is listed in **Table 2.** Also, the parameters of the unit cell of the cubic structure were calculated using the relation,

$$\frac{1}{d^2} = \frac{h^2 + k^2 + l^2}{a^2} \qquad (1)$$

where *d* is the perpendicular distance between (*hkl*) planes. The unit cell parameters of the cubic structure are plotted against the molar percent (x) of Bi, which follows Vegard's law (Jacob et al. 2007) and increases linearly with the Bi atomic ratio owing to replacing the small ion size Sn^{2+} of 0.83 Å with a large Bi^{3+} ion size of 1.17 Å, as can be seen in **Fig. 6**. Furthermore, $Bi_{2.95}Sn_{0.1}S_{4.5}$ showed peaks indexing with orthorhombic ICSD 89323, which is consistent with Bi_2S_3 of the *PNMA* space group with refined unit cell parameters as depicted in **Table 2** and with an average $\Delta(2\theta\ ^o)$ of 0.018 ^{o}.

Optical properties of $Bi_xSn_{6-2x}S_y$ nanopowders

The spectroscopy of the optical absorption of the $Bi_xSn_{6-2x}S_y$ nanopowders is displayed in **Fig. 7**(a, b). The spectra were changed from diffuse reflectance spectra and Kubelka-Munk transformation was accomplished to determine the band gap energy. The optical properties of

$Bi_xSn_{6-2x}S_y$ nanomaterials were obtained by evaluating the optical band gap (E_{bg}). The optical E_{bg} values for $Bi_xSn_{6-2x}S_y$ were estimated using the Kubelka-Munk expression (Pankove 1971):

$$(\alpha\, h\, \nu)^n = K\,(h\,\nu - E_{bg}) \qquad (2)$$

where α is the absorption coefficient, h is the Planck constant, ν is the frequency, K is a constant, and the exponent n has the value of 2 or ½ for direct and indirect transition, respectively. The band gap can be detected as direct or indirect via plotting $(\alpha h\nu)^2$ or $(\alpha h\nu)^{0.5}$ against the photon energy ($h\nu$). **Fig. 7**(a, b) obtained by plotting the square of Kubelka-Munk function $(\alpha h\nu)^2$ vs. $h\nu$, confirms that as-synthesized $Bi_xSn_{6-2x}S_y$ QDs display well-behaved linearity. This affirms that all $Bi_xSn_{6-2x}S_y$ semiconductors attain the direct transition of the energy band and the optical band gap (E_{bg}) can be obtained by extrapolating the linear segment as shown in **Fig. 7**(a, b). The value of the optical band gap for SnS is 1.25 eV, while its values for $Bi_{0.3}Sn_{5.34}S_{5.8}$, $BiSn_4S_{4.5}$, $Bi_{2.14}Sn_{1.71}S_{4.7}$, and $Bi_{2.95}Sn_{0.1}S_{4.5}$ are, respectively, 1.46 eV, 1.44 eV, 1.42 eV, and 1.41 eV. Indeed, the band gap of $Bi_xSn_{6-2x}S_y$ depends greatly on the gap values for tin sulfide (1.3 eV) and bismuth sulfide (1.5 eV) (Wang et al. 2009), where they possess E_{bg} ranging between the two values for SnS and Bi_2S_3. Besides, the gap values for $Bi_xSn_{6-2x}S_y$ linearly increase with the molar ratio (x) of Bi, which may be attributed to: (i) redistribution of orbitals and their electrons caused by the disparity in electronegativity of Sn and Bi ions, (ii) change in (Sn/Bi) stoichiometry varies the crystal lattice and influences the band structure, and (iii) change of inner structure due to cations-anions arrangement including different located elements, the bond angles, and bond length (Khadka and Kim 2014). We have also measured the photoluminescence (PL) quantum yield of the two samples $BiSn_4S_{5.5}$ and $Bi_{0.3}Sn_{5.34}S_{5.8}$ using an integrating sphere purged with nitrogen. **Fig. 8** reveals a clear enhancement in the response of the first sample by about four times that of the second one, when the QDs film was

excited at 550 nm. This indicates the higher efficiency of the $BiSn_4S_{5.5}$ QDs for absorbing incident light whose energy is higher than the band gap energy of the semiconductor.

To recapitulate, the absorption spectra of our synthesized $Bi_xSn_{6-2x}S_y$ semiconductors were measured at room temperature and the spectra are all characterized by a direct band gap with an absorption coefficient of 10^4 - 10^5 cm^{-1}. The absorption coefficient was calculated according to the following equation:

$$\alpha = 2.33A/\varrho \quad (3)$$

where A is the absorbance and ϱ is the thickness of the $Bi_xSn_{6-2x}S_y$ film. The absorption coefficient is greater than 10^5 cm^{-1} for photon energy more than 0.5 eV, which is higher than those for the reported counterparts CIGS ($CuIn_{1-x}Ga_xSe_2$) and CZTS (Cu_2ZnSnS_4) absorbers. A thickness of 300 nm from $Bi_xSn_{6-2x}S_y$ QDs can absorb ~ 99% of incident photons, which is simply greater than the band gap owing to the substantially high absorption coefficient. Such values of the band gap are near-optimal harvesting 1.5 eV of solar energy conversion (Aldalbahi et al. 2016), likely due to the quantum size effect that produces ideal absorbing materials. In addition, the excited electrons can be generated from the sulfide orbitals. The absorption spectra of as-prepared $Bi_xSn_{6-2x}S_y$ presented in the inset of **Fig. 7**(b), are covered the whole UV-visible wavelength from 200 to 900 nm and thus can offer the opportunity to use most of the solar spectrum for photocatalysis or photovoltaic applications. Such results indicate enhanced conversions of solar energy by our designed materials. Besides, the lattice disorder, change of component arrangement, and inclusion of impurities all have a profound effect on the optical absorption of our developed $Bi_xSn_{6-2x}S_y$ QDs (Fischereder et al. 2010).

Electronic behavior of $Bi_xSn_{6-2x}S_y$ QDs

Mott-Schottky analysis was exploited to scrutinize the electronic properties of the as-synthesized $Bi_xn_{6-2x}S_y$ semiconductors QDs by measuring the interfacial capacitance (C) between the semiconductor and sodium sulfate electrolyte over the potential window -0.6 to

0.9 V (vs. Ag/AgCl). The mott-Schottky relation (Eq. 4) was applied to estimate the flat band potential (E_{fb}) and the n- or p-type fictional character of each semiconductor, as well as its charge carrier density (N_D) as follows (Breault and Bartlett 2012; Heakal et al. 2018a,b; Heakal and Shehata 2020):

$$\frac{1}{C^2} = \frac{2}{\varepsilon\varepsilon_0 A^2 e N_D}\left(E - E_{fb} - \frac{kT}{e}\right) \quad (4)$$

where E and E_{fb} are the applied potential and flat band potentials, respectively, C is the interfacial capacitance, ε is the dielectric constant of the semiconductor, A is the area of the working electrode, k is the Boltzmann's constant, ε_o is the permittivity of the free space (8.854×10^{-14} F cm^{-1}), e is the electronic charge, N_D is the charge carrier density, and T is the absolute temperature. By plotting C^{-2} versus the applied potential E, the slope of this plot is commonly used to calculate the free carrier donors' concentration:

$$N_D = \frac{2}{\varepsilon\varepsilon_0 A^2 e\ (\text{slope})} \quad (5)$$

The flat-band potential can also be calculated from the intercept of the plot and its slope:

$$E_{fb} = -\left[\frac{(\text{Intercept})}{(\text{slope})} + \frac{kT}{e}\right] \quad (6)$$

where the factor ($\frac{kT}{e}$) can be neglected as it has a very small quantity of only 25 mV at room temperature (298 K).

Fig. 9 shows Mott-Schottky plots for the as-prepared SnS, $Bi_{0.3}Sn_{5.34}S_{5.8}$, $BiSn_4S_{5.5}$, $Bi_{2.14}Sn_{1.71}S_{4.7}$, and $Bi_{2.95}Sn_{0.1}S_{4.5}$ nanomaterials. The E_{fb} of these five semiconductors are estimated to be, -0.18 V, -0.42 V, -0.53 V, -0.51 V and +0.66 V (vs. Ag/AgCl), respectively. On the one hand, for the four p-type semiconductors, the E_{fb} value is clearly shifted towards a more negative potential from -0.18 to -0.53 V with increasing the Bi content owing to the upward movements of the Fermi level. The cathodic shift of E_{fb} obtained by the four p-type $Bi_xSn_{6-2x}S_y$ semiconductors can be attributed to the significant increase in electron density,

which moves the Fermi level upward to the conduction band and greatly decreases carrier recombination (Jing et al. 2014). Additionally, the cathodic shift of E_{fb} for $Bi_xSn_{6-2x}S_y$ semiconductors can be attributed to the efficient transport of the hole by Bi^{3+} dopant, which improves the conductivity leading to the high ability of carrier migration and enhances photovoltaic activity under UV-visible light irradiation. On the other hand, E_{fb} of the n-type $Bi_{2.95}Sn_{0.1}S_{4.5}$ semiconductor is a positive value of + 0.66 V (see **Fig. 9**e).

Regarding the charge carrier density (N_D) of $Bi_xSn_{6-2x}S_y$ semiconductors, **Fig. 10** reveals that its value increases exponentially with the molar ratio of Bi (x) in the semiconductors. The charge carrier densities of SnS, $Bi_{0.3}Sn_{5.34}S_{5.8}$, $BiSn_4S_{5.5}$, $Bi_{2.14}Sn_{1.71}S_{4.7}$, and $Bi_{2.95}Sn_{0.1}S_{4.5}$ are found to be 2.214 x 10^{24}, 3.16 x10^{25}, 1.455x 10^{28}, 0.6428 x 10^{29}, and 2.084 x10^{29} m^{-3}, respectively. The increase in N_D value of $Bi_xSn_{6-2x}S_y$ with Bi content in semiconductor can be ascribed to the increase of defects density in their nanostructures (Lei et al. 2009). The doping with cations of higher oxidation states such as Ti^{4+} and Bi^{3+} can develop electron concentration by working as donor dopants (Fang et al. 2010). This effect improves the charge carrier density and directly increases the conductance of semiconductors and lessens their impedance, as will be confirmed by the EIS method in the next part. Therefore, rising Bi content encourages electrical conductivity and increases the lifetime of photogenerated hole/electron via effective charge separation, which boosts the harvest of solar energy of $Bi_xSn_{6-2x}S_y$ semiconductors. Mott-Schottky analysis reveals that N_D values for p- and n-type semiconductors can be estimated, respectively, via Eq. 5 from the negative and positive slopes of the plots in **Fig. 9**. The high N_D values are because of the high defect density on the surface of the semiconductors QDs (Lei et al. 2009). The increase in charge carrier density may be explained by the higher number of sulfide vacancies in the $Bi_xSn_{6-2x}S_y$ semiconductors, which are the primary source of free conduction band electrons in semiconductors QDs (Kempken et al. 2015). Indeed, the

flat band potential and charge carrier density both values prove that $Bi_XSn_{6-2X}S_y$ QDs are the most auspicious semiconductors absorbers for photocatalytic applications.

Photocatalytic Activity and Mechanism of $Bi_xSn_{6-2x}S_y$ photocatalysts

Typically, the photocatalytic activity of a photocatalyst is affected by the efficiency of electron/hole pairs separation, charge carriers transport, and production of photoinduced electrons/holes (Gao et. al. 2018). Bulk electrolysis has been performed to investigate the photocurrent-time response, which elucidates the electron/hole separation dynamics. **Fig. 11**b-f displays the photocurrent-time characteristics at a potential of 0.650 V (vs. Ag/AgCl) for the as-prepared different $Bi_xSn_{6-2x}S_y$ QDs electrodes. In general, the photocurrent was found to increase more significantly under light than in the dark. Additionally, under UV-vis irradiation, Fig. 11a shows that the photocurrent became progressively more negative as the Bi content increased in the photocatalyst. This behavior confirms that Bi doping has a substantial effect on the improvement of the light harvesting of our photocatalyst material. For $Bi_{0.3}Sn_{5.34}S_{5.8}$, $Bi_{0.4}Sn_{5.5}S_6$, $BiSn_4S_{5.5}$, $Bi_{2.95}Sn_{0.1}S_{4.5}$, and $Bi_{2.14}Sn_{1.71}S_{4.7}$ samples, the photocurrent density achieves, respectively, the following values -33, -35, -44, -47, and -47.5 mA cm^{-2}. The EIS technique was also utilized for further realizing the charge transfer resistance and to illuminate processes of photoexcited electron/hole pairs relocation. The Nyquist plots of the $Bi_{0.3}Sn_{5.34}S_{5.8}$, $Bi_{0.4}Sn_{5.5}S_6$, $BiSn_4S_{5.5}$, $Bi_{2.95}Sn_{0.1}S_{4.5}$, and $Bi_{2.14}Sn_{1.71}S_{4.7}$ samples are presented in **Fig. S1**. The impedance spectrum of each sample consists of a single semicircle at medium and low-frequency regions related to the charge transfer resistance (R_{ct}) and double layer capacitance (C_{dl}) of the specified QD electrode. This behavior confirms a charge transfer mechanism, and as found, the $BiSn_4S_{5.5}$ catalyst has the smallest half-circle size compared to the others under conditions of darkness and illumination. The experimental EIS data were all fitted to the appropriate Randles circuit model displayed as an inset in **Fig. S1** and the estimated circuit parameters are detailed in **Table 4**. The equivalent circuit model comprises the solution

resistance (R_s) linked in series to the parallel combination of the time constant $R_{ct}C_{dl}$. Indeed, the lowest R_{ct} value of 0.69 Ω cm^2 obtained by $BiSn_4S_{4.5}$ photocatalyst indicates the lowest interfacial resistance for the charge transport (Tian et al. 2015; Tayyab et al. 2022a,b; Liu et al. 2021; Djellabi et al. 2021; Liu et al. 2021; Hosseini et al. 2022), hence the fastest transfer of the electron/hole pairs. The results generally reveal that the photo-generated charge carriers of the $BiSn_4S_{5.5}$ photocatalyst are actually split more than the situation detected by other $Bi_XSn_{6-2X}S_y$ semiconductors QDs. $BiSn_4S_{5.5}$ photocatalyst material possesses a stable and high photocurrent density, characterized by the lowest recombination rate of the electron/hole pairs and the highest charge transfer mechanisms. These possessions confirm a great improvement in the motion of the photogenerated electron/hole pairs, a high efficiency of photodegradation, and a lower kinetic barrier (Hosseini et al. 2022). Likewise, the slow recombination rate of electrons/holes in the $BiSn_4S_{4.5}$ photocatalyst is certainly influenced by the d-spacing of planes and the arrangement of ions inside its unit cell. The second and third planes in this active photocatalyst (**Fig. 5c**) shifted and their peaks were obviously enlarged, which means a new arrangement of ions. The d-spacing of crystal planes can support rapid charge transfer, which efficiently slows charge recombination and augment photodegradation efficacy. In addition, the intensity of ions in these planes can increase the adsorption of polluting molecules with a subsequent improvement in the rate of their photodegradation.

The removal of organic pollutants is essential for environmental sanitation and this can be done simply by using photocatalytic degradation via nanostructured semiconductors under absorption of the solar spectrum. Aqueous media used in cotton, wool, and silk industries are usually contaminated with the highly water-soluble MB, which is considered a potentially hazardous and carcinogenic organic dye (Biacchi et al. 2013), and hardly degrades using visible light (Khan et al. 2022). The photoelectrochemical activity of $Bi_xSn_{6-2x}S_y$ photocatalysts was assessed using photodegradation of MB under UV-visible and visible light irradiation. **Fig. 12**

shows the absorption spectra of MB at different decomposition times using $Bi_xSn_{6-2x}S_y$ semiconductor QDs. The intense absorption of MB is at about λ_{max} of 663 nm and the height of the peak is drastically decreased by prolonging the irradiation time. Under UV-visible irradiation, the synthesized $BiSn_4S_{5.5}$ semiconductor QDs with a dose of 20 mg/100 mL were found to photodegrade 10^{-4} M MB solution within 10 min only (**Fig. 12**c), which is considered the shortest photodegradation time in comparison to the reported results in the literature, as shown in **Table 5** (Liu et al. 2014; Fu et al. 2021; Kumar et al. 2021; Ajithkumar et al. 2020; Demir et al. 2020; Baytar et al. 2018; Horoz et al. 2018; Gao et al. 2018; Gayathri et al. 2019; Ramki et al. 2020; Zhang et al. 2020; and Raju et al. 2021). This is because the $BiSn_4S_{5.5}$ photocatalyst possesses efficient separation of electrons/holes. However, the MB's photodegradation time increased to 60 min when using the same $BiSn_4S_{5.5}$ photocatalyst irradiated with visible light. In addition, the other two photocatalysts SnS and $Bi_{0.3}Sn_{5.34}S_{5.8}$ showed a photodegradation time for MB that increased to 210 and 390 min under UV-visible irradiation, respectively (**Fig. 12**a, b). The better capability of $BiSn_4S_{5.5}$ photocatalyst may be caused by the intrinsic arrangement of ions in its grains, the huge surface area of quantum dots, and their electronic properties, which all facilitate the separation of holes/electrons to produce large numbers of superoxide and hydroxyl radicals in the degraded MB molecule (Sun et al. 2012). However, $Bi_{2.14}Sn_{1.71}S_{4.7}$ and $Bi_{2.95}Sn_{0.1}S_{4.5}$ showed relatively slow photodegradation properties for MB due to their low absorption of UV-visible irradiation, decrease in their surface area, and crystal system, as well as the rapid combination rate of electron/hole pairs.

The mechanism of photodegradation of MB with the as-synthesized $Bi_xSn_{6-2x}S_y$ photocatalysts under UV-visible irradiation can involve the excitation of the electrons from the valence band (VB) of $Bi_xSn_{6-2x}S_y$ photocatalysts into the conduction band (CB) leaving holes in the VB. The holes react with hydroxy ions and produce highly active hydroxy radicals. Moreover, electrons react with the adsorbed oxygen and generate O_2^* radicals. Also, electrons

can react with adsorbed oxygen and H^+ to form the highly oxidative H_2O_2, which can initiate a series of oxidation reactions and radicals. Photogenerated radicals and superoxide free radicals play an influential role in the photodegradation behavior of MB with $Bi_xSn_{6-2x}S_y$ photocatalysts. The actively generated OH* rapidly degrades MB due to the large numbers of electron/hole pairs produced in the $Bi_xSn_{6-2x}S_y$ photocatalyst. The mechanism of MB photodegradation can thus be summarized by the following equations (Khan et al. 2022; Seneviratne et al. 2021),

$$Bi_xSn_{6-2x}S_y + h\nu \rightarrow h^+ + e^-$$

$$e^- + O_2 \rightarrow O_2^*$$

$$hole + OH^- \rightarrow OH^*$$

$$2\ e^- + O_2 + 2H^+ \rightarrow H_2O_2$$

$$O_2^* + H_2O_2 \rightarrow OH^- + OH^* + O_2$$

$$MB + OH^* \rightarrow Intermediate \rightarrow CO_2 + H_2O$$

During the photodegradation steps, MB is converted to H_2O, CO_2, Cl^-, and sulfate. The different photodegradation periods of MB on our various $Bi_xSn_{6-2x}S_y$ photocatalysts are probably ascribed to the different arrangement of ions in the planes of the unit cell, their band gap values, light absorbance, the recombination rate of charge carriers, and their different electronic properties, as well as their composition. The small grain size of $Bi_xSn_{6-2x}S_y$ photocatalysts increases the lifetime of hole/electron pairs by decreasing the travel distance to the surface which prevents the recombination of the hole/electron more than bulk semiconductors. Moreover, the high photocatalytic activity may be due to the creation of intra-gap states in the nanostructure (Shen et al. 2014). The photocatalytic activity behavior of $Bi_xSn_{6-2x}S_y$ photocatalysts is shape-dependent and this has been confirmed previously by the nanostructured semiconductors (Negem et al. 2023). In addition, the ability of the photocatalyst to separate the hole/electron is an important factor. $Bi_xSn_{6-2x}S_y$ semiconductors are considered potentially promising photocatalysts. The combination of a high E_{fb} and huge surface area in $BiSn_4S_{4.5}$ QDs leads to superior photocatalytic activity. It is noteworthy that the Sn added Bi_2S_3 material demonstrates enhanced photocatalytic efficiency than a single Bi_2S_3 photocatalyst

(Sharma and Khare 2018). Our $BiSn_4S_{5.5}$ QDs exhibit higher photocatalytic activity to degrade MB than the other most known semiconductors as shown in Table 5. Globally, the results display that the $Bi_xSn_{6-2x}S_y$ photocatalysts can significantly increase the photodegradation efficiency of the MB dye.

Conclusions

In summary, we have used the nanoemulsion approach to synthesize the highly uniform $Bi_xSn_{6-2x}S_y$ semiconductor QDs with a grain size of 2-5 nm, which possess high absorbance of UV-visible light irradiation. The molar ratio of Bi inside the $Bi_xSn_{6-2x}S_y$ QDs varied between 0.33 and 2.95 nm. $Bi_xSn_{6-2x}S_y$ sQDs can be arranged in crystalline structures of cubic or orthorhombic. The optical, photocatalytic activity and electronic properties of $Bi_xSn_{6-2x}S_y$ semiconductors greatly depend on the composition and morphological structure of the QDs. All $Bi_xSn_{6-2x}S_y$ semiconductor materials display the direct band gap (E_{bg}) and E_{fb} values. The most active photocatalyst is $BiSn_4S_{5.5}$ which can photodegrade 10^{-4} M MB solution in only 10 min. The E_{fb} values of $Bi_xSn_{6-2x}S_y$ semiconductors are greatly affected by composition and structure and increased by doping with Bi ions. As anticipated, the enhanced transport of photogenerated electron/hole pairs has been achieved as a result of the nanostructure, band gap energy (i.e. trap density), as well as internal resistance minimization, which is responsible for the high photocatalytic performance. The synthesized $Bi_xSn_{6-2x}S_y$ semiconductors can harvest the most solar spectrum using low-cost elements which are promising for potential applications as photocatalysts.

Acknowledgment

The authors would like to thank Fayoum University, Cairo University, and the University of St Andrews, for the facilities provided during this work.

Supplementary Information Some obtained data during this work are included in the supplementary information.

Ethical Approval The manuscript is prepared in compliance with the Publishing Ethics Policy.

Consent to participate Not applicable.

Consent to Publish Not applicable.

Author Contributions **MR Negem** and **D Miller:** Conceptualization and design, Investigation, Methodology, Resources, Formal analysis, Data curation, Writing-original draft. **J Irvine:** Conceptualization and design, Writing-review & editing. **FET Heakal:** Conceptualization and design, Writing-original draft, Writing-reviewing & editing, corresponding author.

Funding Open access funding is provided by the Science, Technology & Innovation Funding Authority (STDF) in cooperation with the Egyptian Knowledge Bank (EKB). Not applicable.

Competing Interests The authors declare no competing interests.

Availability of data and materials Data and materials will be available upon request from the corresponding author.

References

Ajithkumar P, Mohana S, Sumathi S (2020) Synthesis, characterization, optical and photocatalytic activity of yttrium and copper co-doped zinc ferrite under visible light. J Mater Sci: Mater Electron 31:1168-1182. https://doi.org/10.1007/s10854-019-02628-8

Aldalbahi A, Mkawi E, Ibrahim K, Farrukh M (2016) Effect of sulfurization time on the properties of copper zinc tin sulfide thin films grown by electrochemical deposition. Sci Rep 6:32431. https://doi.org/10.1038/srep32431

Antunez P, Torelli D, Yang F et al (2014) Low-temperature solution-phase deposition of SnS thin films. Chem Mater 26: 5444−5446. https://doi.org/10.1021/cm503124u

Baytar O, Sahin O, Kilicvuran H, Horoz S (2018) Synthesis, structural, optical and Photocatalytic properties of Fe-alloyed CdZnS nanoparticles. J Mater Sci: Mater Electron 29:4564-4568. https://doi.org/10.1007/s10854-017-8406-0

Bernechea M, Cao Y, Konstantatos G (2015) Size and bandgap tunability in Bi_2S_3 colloidal nanocrystals and its effect in solution processed solar cells. J Mat Chem A 3:20642-20648. https://doi. 10.1039/C5TA04441C

Biacchi A, Vaughn D, Schaak R (2013) Synthesis and Crystallographic Analysis of Shape-Controlled SnS Nanocrystal Photocatalysts: Evidence for a Pseudotetragonal Structural Modification. J Am Chem Soc 135:11634−11644. https://doi.org/10.1021/ja405203e

Breault T, Bartlett B (2012) Lowering the Band Gap of Anatase-Structured TiO_2 by Coalloying with Nb and N: Electronic Structure and Photocatalytic Degradation of Methylene Blue Dye. J Phys Chem C 116:5986−5994. https://doi.org/10.1021/jp2078456

Cassette E, Pons T, Bouet C et al (2010) Synthesis and characterization of near-infrared Cu−In−Se/ZnS core/shell quantum dots for in vivo imaging. Chem. Mater. 22, 6117-6124. doi.org/10.1021/cm101881b

Chao J, Xie Z, Duan X et al (2012) Visible-light-driven photocatalytic and Photoelectrochemical properties of porous SnS_x(x =1,2) architectures. Cryst Eng Comm 14:3163. https://doi. 10.1039/C2CE06586J

Demir H, Şahin Ö, Baytar O, Horoz S (2020) Investigation of the properties of photocatalytically active Cu-doped Bi_2S_3 nanocomposite catalysts. J Mater Sci: Mater Electron 31:10347-10354. https://doi.org/10.1007/s10854-020-03582-6

Djellabi R, Giannantonio R, Falletta E, Bianchi C (2021) SWOT analysis of photocatalytic materials towards large scale environmental remediation. Current Opinion in Chemical Engineering 33:100696. https://doi.org/10.1016/j.coche.2021.100696

Fang F, Chen L, Chen Y, Wu L (2010) Synthesis and Photocatalysis of $ZnIn_2S_4$ Nano/Micropeony. J Phys Chem C 114:2393-2397. https://doi.org/10.1021/jp910291p

Fischereder A, Rath T, Haas W et al (2010) Investigation of Cu_2ZnSnS_4 Formation from Metal Salts and Thioacetamide. Chem Mater 22:3399–3406. https://doi.org/10.1021/cm100058q

Fu Y, Wang Y, Zhao H, et al. (2021) Synthesis of ternary ZnO/ZnS/MoS_2 piezoelectric Nanoarrays for enhanced photocatalytic performance by conversion of dual heterojunctions. Appl Surf Sci 556:149695. https://doi.org/10.1016/j.apsusc.2021.149695

Gao H, Mo Z, Guo R, Niu X, Li Z (2018) Formation of snowflake-like CdS/reduced Graphene oxide composite for efficient photocatalytic organic dye degradation. J Mater Sci: Mater Electron 29:5944-5953. https://doi.org/10.1007/s10854-018-8567-5

Gayathri GD, Manikandan K, Thiruneelakandan R (2019) Preparation and effect of complexing agents on ternary FeZnS2 thin films by chemical bath deposition method for photo catalytic degradation of dye molecules. J Mater Sci: Mater Electron 30:6023-6036. https://doi.org/10.1007/s10854-019-00903-2

Gelbart W, Ben-Shaul A, (1996) The "New" Science of "Complex Fluids". J Phys Chem 100:13169–13189. https://doi.org/10.1021/jp9606570

Gerein N, Haber J (2006) One-Step Synthesis and Optical and Electrical Properties of Thin Film Cu_3BiS_3 for Use as a Solar Absorber in Photovoltaic Devices. Chem Mater 18:6297-6302. https://doi.org/10.1021/cm061453r

Gupta, RK, Nguyen TA, Yasin G (Eds.) (2022) Metal-Organic Framework-Based Nanomaterials for Energy Conversion and Storage. Elsevier.

Heakal F El-Taib, Abd-Ellatif WR, Tantawy NS, Taha AA (2018a) Characterization of electrodeposited undoped and doped thin ZnO passive films on zinc metal in alkaline HCO_3^-/CO_3^{2-} buffer solution. RSC adv 8:39321-39333. https://doi: 10.1039/C8RA06899B

Heakal F El-Taib, Abd-Ellatif WR, Tantawy NS, Taha AA (2018b) Impact of pH and temperature on the electrochemical and semiconducting properties of zinc in alkaline buffer media. RSC adv 8:3816-3827. https://doi: 10.1039/C7RA12723E

Heakal F El-Taib, Shehata OS (2020) Insight into the electrochemical and semiconducting properties of native oxide films on Ti metal and its Ti–6Al–4V alloy in borate buffer solutions. Prot Met Phys Chem Surf 56:333-342. https://doi.org/10.1134/S2070205120020082

Hosseini F, Assadi A, Nguyen-Tri P, Imran Ali I, Rtimi S(2022) Titanium-based photocatalytic coatings for bacterial disinfection: The shift from suspended powders to catalytic interfaces. Surfaces and Interfaces 32:102078. https://doi.org/10.1016/j.surfin.2022.102078

Horoz S, Baytar O, Sahin O, Kilicvuran H (2018) Photocatalytic degradation of methylene blue with Co alloyed CdZnS nanoparticles. J Mater Sci: Mater Electron 29:1004-1010. https://doi.10.1007/s10854-017-7999-7

Huang H, Zhu J (2013) The electrochemical applications of quantum dots. Analyst 138:5855-5865. https://doi. 10.1039/C3AN01034A

Jacob KT, Raj S, Rannesh L (2007) Vegard's law: a fundamental relation or an

approximation? Inter J Mater Res 98:776-779. https://doi.org/10.3139/146.101545

Jing H, Wang C, Zhang Y et al (2014) Photocatalytic degradation of methylene blue in ZIF-8. RSC Adv 4:54454-54462. https://doi. 10.1039/C4RA08820D

Kempken B, Dzhagan V, Zahn D et al (2015) Synthesis, optical properties, and photochemical activity of zinc-indium-sulfide nanoplates. RSC Adv 5:89577-89585. https://doi: 10.1039/C5RA20570K

Khadka D, Kim J (2014) Structural Transition and Band Gap Tuning of Cu2(Zn,Fe)SnS4 Chalcogenide for Photovoltaic Application. J Phys Chem C 118:14227−14237. https://doi.org/10.1021/jp503678h

Khan I, Saeed K, Zekker I et al (2022) Review on methylene blue: its properties, uses, toxicity and photodegradation. Water 14:242- 272. https://doi.org/10.3390/w14020242

Kumar M., Singh G., Vaish R. (2021). A reduced graphene oxide/bismuth vanadate composite as an efficient piezocatalyst for degradation of organic dye. Mater. Adv. 2:4093-4101. https://doi.10.1039/d1ma00284h

Lei Y, Song S, Fan W et al (2009) Facile Synthesis and Assemblies of Flowerlike SnS_2 and In^{3+}-Doped SnS_2: Hierarchical Structures and Their Enhanced Photocatalytic Property. J Phys Chem C 113:1280-1285. https://doi.org/10.1021/jp8079974

Li H, Ji J, Zheng X et al (2015) Preparation of SnS quantum dots for solar cells application by an in-situ solution chemical reaction process. Mater Sci in Semiconductor Processing 36:65-70. https://doi.org/10.1016/j.mssp.2015.03.036

Li S, Zheng J, Hu Z et al (2015) 2D hybrid anode based on SnS nanosheet bonded with graphene to enhance electrochemical performance for lithium-ion batteries. RSC Adv 5:46941−46946. https://DOI: 10.1039/C5RA07292A

Lim J, Lee W, Nam M et al (2011) InP@ ZnSeS, core@ composition gradient shell quantum Dots with enhanced stability. Chem Mater 23:4459-4463. https://doi.org/10.1021/cm201550w

Liu G, Feng M, Tayyab M, Gong J, Zhang M, Yang M, Lin K(2021) Direct and efficient reduction of perfluorooctanoic acid using bimetallic catalyst supported on carbon. Journal of Hazardous Materials 412:) 125224. https://doi.org/10.1016/j.jhazmat.2021.125224

Liu J, Zhang D, Pu X et al (2014) Combustion synthesis of $Zn_{1-x}Cd_xS$ and its

photodegradation performance of methylene blue. Mater Lett 117:158-161. https://doi.org/10.1016/j.matlet.2013.11.128

Liu L, Chen X (2014) Titanium Dioxide Nanomaterials: Self-Structural Modifications. Chem Rev 114:9890. https://doi.org/10.1021/cr400624r

Liu X, Li Y, Zhou B et al (2014) Shape-controlled synthesis of SnE (E = S, Se) semiconductor nanocrystals for optoelectronics. Chem Mater 26:3515−3521. https://doi.org/10.1021/cm501023w

Liu Y, Zhu Q, Tayyab M, Zhou L, Lei J, Zhang J(2021) Single-Atom Pt Loaded Zinc Vacancies ZnO–ZnS Induced Type-V Electron Transport for Efficiency Photocatalytic H2 Evolution. Sol. RRL 2021, 5, 2100536. DOI: 10.1002/solr.202100536

Mora-sero I, Gimenez S, Fabregat-Santiago F et al (2009) Recombination in quantum dot sensitized solar cells. Acc Chem Res 42: 1848-1857. https://doi.org/10.1021/ar900134d

Nady H, Negem M (2016) Ni–Cu nano-crystalline alloys for efficient electrochemical Hydrogen production in acid water. RSC Adv 6:51111-51119. https://doi. 10.1039/C6RA08348J

Negem M, Elzyat M, Saad I, Shaban M (2023) Novel absorber of SHg_xZn_{1-x} QDs ($0.05 \leq x \leq 0.8$) for UV-visible-IR irradiation synthesized using W/O nanoemulsion for photovoltaic applications. Under submission.

Negem M, Nady H (2020) Benchmark Electrocatalysis Activity of 3D-Ni-Co-TiO_2 Nanocomposites for Hydrogen Fuel Production Via Alkaline Electrolytes. J Mater Eng Perform 29:6940-6951. https://doi.org/10.1007/s11665-020-05180-3

Nguyen T, Michael M, Mulvaney P (2014) Synthesis of highly crystalline CdSe@ ZnO nanocrystals via monolayer-by-monolayer epitaxial shell deposition. Chem. Mater. 26, 4274−4279. https://doi.org/10.1021/cm501858s

Niezgoda J, Harrison M, McBride J, Rosenthal S (2012) Novel Synthesis of Chalcopyrite $Cu_xIn_yS_2$ Quantum Dots with Tunable Localized Surface Plasmon Resonances. Chem Mater 24:3294−3298. https://doi.org/10.1021/cm3021462

Pankove JI (1971) Optical Processes in Semiconductors Englewood Cliffs: Prentice-Hall Inc.

Raju P, Jesuraj JP, Muthukumaran S (2021) Influence of Ni^{2+} ions on the structural, morphological, photoluminescence, photo-catalytic and anti-bacterial studies of $Cd_{0.9}Zn_{0.1}S$ nanostructures. J Mater Sci: Mater Electron 32:14310-14327. https://doi.org/10.1007/s10854-021-05994-4

Ramki K, RajaPriya A, Sakthivel P et al (2020) Rapid degradation of organic dyes under sunlight using tin-doped ZnS nanoparticles. J Mater Sci: Mater Electron 31:8750-8760. https://doi.org/10.1007/s10854-020-03410-x

Sanchez-Dominguez M, Pemartin K, Boutonnet M, (2012) Preparation of inorganic nanoparticles in oil-in-water microemulsions: A soft and versatile approach. Curr Opin in Colloid Inter Sci 17: 297. https://doi.org/10.1016/j.cocis.2012.06.007

Seneviratne KL, Munaweera I, Peiris S (2021) Recent progress in visible-light active (VLA) TiO_2 nano-structures for enhanced photocatalytic activity (PCA) and antibacterial properties: a review. Iranian J Catal 11:217-245. http://ijc.iaush.ac.ir/article_685574.html

Sharma S, Khare N (2018) Sensitization of narrow band gap Bi_2S_3 hierarchical nanostructures with polyaniline for its enhanced visible-light photocatalytic performance. Colloid Polym. Sci. 296:1479. https://doi.org/10.1007/s00396-018-4362-3

Shen S, Zhou J, Dong C et al. (2014) Surface Engineered Doping of Hematite Nanorod Arrays for Improved Photoelectrochemical Water Splitting. Sci Rep 4:6627. https://doi.org/10.1038/srep06627

Sun Y, Cheng H, Gao S et al. (2012) Freestanding Tin Disulfide Single-Layers Realizing Efficient Visible-Light Water Splitting. Angew Chem Int Ed 51:1-6. https://doi.org/10.1002/anie.201204675

Tayyab M, Liu Y, Min S, Irfan R, Zhu Q, Zhou L, Lei J, Zhang J (2022) Simultaneous hydrogen production with the selective oxidation of benzyl alcohol to benzaldehyde by a noble-metal-free photocatalyst VC/CdS nanowires. Chinese Journal of Catalysis 43: 1165–1175. DOI: 10.1016/S1872-2067(21)63997-9

Tayyab M, Liu Y, Liu Z, Pan L, Xu Z, Yue W, Zhou L, Lei J, Zhang J, (2022) One-pot in-situ hydrothermal synthesis of ternary In2S3/Nb2O5/Nb2C Schottky/S-scheme integrated heterojunction for efficient photocatalytic hydrogen production. Journal of Colloid and Interface Science 628: 500–512. https://doi.org/10.1016/j.jcis.2022.08.071

Tian N, Huang H, Liu C, Dong F, Zhang T, Du X, Yu S, Zhang Y(2015) n-situ co-pyrolysis fabrication of CeO2/g-C3N4 n-n type heterojunction for synchronously promoting the photo-induced oxidation and reduction properties. J. Mater. Chem. A, 2015,3, 17120-17129. https://doi.org/10.1039/C5TA03669K

Wang Y, Chen J, Wang P, et al (2009) Syntheses, Growth Mechanism, and Optical Properties of [001] Growing Bi_2S_3 Nanorods. J Phys Chem C 113:16009-16014. https://doi.org/10.1021/jp904448k

Xu X, Randorn C, Efstathiou P, Irvine JTS (2012) A red metallic oxide photocatalyst. Nature Mater 11:595-598. https://doi.org/10.1038/nmat3312

Zhang M, Xin X, Feng Y et al (2022) Coupling Ni-substituted polyoxometalate catalysts with water-soluble CdSe quantum dots for ultra-efficient photogeneration of hydrogen under visible light. Appl Catal B: Environmental 303:120893. https://doi.org/10.1016/j.apcatb.2021.120893

Zhang Q, Wang Y, Su Y et al (2020) CdS-decorated surface-coarsened TiO_2 nanobelts with enhanced visible-light photocatalytic performances. J Mater Sci: Mater Electron 31: 4931-4942. https://doi.org/10.1007/s10854-020-03059-6

Table 1 The amounts of different chemicals utilized in the synthesis of $Bi_xSn_{6-2x}S_y$ nanomaterials

Metal Sulphide	$SnCl_2$ (g)	Bi_2O_3 (g)	Na_2S (g)	H_2O (mL)	HCl (mL)	Isohexane (mL)	Propanol (mL)	SLS (g)
SnS	2.24	-	2.30	125	5	75	50	75
$Bi_{0.33}Sn_{5.34}S_{5.8}$	1.42	0.08	1.63	125	5	75	50	50
$Bi_{0.4}Sn_{5.5}S_6$	1.53	0.12	1.86	125	5	75	50	50
$BiSn_4S_{5.5}$	1.62	0.13	2.43	125	5	75	50	50
$Bi_{2.14}Sn_{1.71}S_{4.7}$	0.18	0.77	2.01	125	10	75	50	50
$Bi_{2.95}Sn_{0.1}S_{4.5}$	0.13	1.19	1.58	125	13	75	50	50

Table 2 Parameters of the unit cell of nanostructured $Bi_xSn_{6-2x}S_y$

Metal Sulphide	a /Å	b / Å	c / Å	υ / $Å^3$
SnS	5.997	-	-	215.67
$Bi_{0.3}Sn_{5.34}S_{5.8}$	6.012	-	-	217.29
$BiSn_4S_{5.5}$	6.021	-	-	218.27
$Bi_{2.14}Sn_{1.71}S_{4.7}$	6.037	-	-	220.02
$Bi_{2.95}Sn_{0.1}S_{4.5}$	11.179	11.276	3.970	500.43

Table 3 values for charge carrier density, optical band gap, photodegradation time, and flat band potential obtained for $Bi_xSn_{6-2x}S_y$ semiconductor QDs.

Metal sulphide	Optical band gap (E_{bg}) / eV	Photodegradation time/ min	Flat band potential (E_{fb}) / V	Charge carrier density (N_D) / m^{-3}
SnS	1.25	210	-0.18	2.214×10^{24}
$Bi_{0.3}Sn_{5.34}S_{5.8}$	1.46	180	-0.42	3.160×10^{25}
$BiSn_4S_{5.5}$	1.44	10	-0.53	1.455×10^{28}
$Bi_{2.14}Sn_{1.71}S_{4.7}$	1.42	480	-0.51	6.428×10^{28}
$Bi_{2.95}Sn_{0.1}S_{4.5}$	1.41	580	+0.66	2.084×10^{29}

*The estimate error of $E_{bg} \pm 0.1$ eV and of $E_{fb} \pm 0.1$ V.

Table 4 Equivalent circuit data of the EIS measurements recorded at 0.65 V on the different cathodes in 0.6 M Na_2SO_4 at room temperature

photocatalysts	R_s/ Ω	R_{ct}/ Ω cm^2	C_{dl}/ mF cm^{-2}
$Bi_{0.3}Sn_{5.34}S_{5.8}$	1.69±0.001	0.83±0.0005	2.85±0.007
$Bi_{0.4}Sn_{5.5}S_6$	4.23±0.006	2.42±0.003	1.84±0.008
$BiSn_4S_{5.5}$	1.89±0.007	0.69±0.006	7.17±0.003
$Bi_{2.14}Sn_{1.71}S_{4.7}$	3.24±0.002	1.17±0.004	3.15±0.004
$Bi_{2.95}Sn_{0.1}S_{4.5}$	2.21±0.002	0.82±0.0069	6.65±0.001

Table 5 The comparison of different photocatalysts for photodegradation of methylene blue

Photocatalyst	Amount of photocatalyst/volume of the dye	Mass of MB (mg/L)	Photodeg-radation time (min)	Reference
$Zn_{1-x}Cd_xS$	20 mg / 50 mL	20	120	(Liu et al 2014)
ZnO/ZnS/MoS_2	10 mg / 50 mL	10	50	(Fu et al 2021)
rGO/$BiVO_4$	50 mg / 50 mL	5	180	(Kumar et al 2021)
$Cu_yZn_{1-y}Fe_{2-x}Y_xO_4$	10 mg / 50 mL	10	180	(Ajithkumar et al 2020)
Cu-doped Bi_2S_3	10 mg / 50 mL	20	110	(Demir et al 2020)
Fe-alloyed CdZnS	30 mg / 50 mL	25	90	(Baytar et al 2018)
Co(5%):CdZnS NPs	30 mg / 50 mL	25	100	(Horoz et al 2018)
CdS/rGO	50 mg / 50 mL	12	140	(Gao et al 2018)
$FeZnS_2$	20 mg / 20 mL	20	60	(Gayathri et al 2019)
Tin‑doped ZnS	100 mg / 100 mL	20	180	(Ramki et al 2020)
CdS-decorated TiO_2	30 mg /100 mL	20	200	(Zhang et al 2020)
$CdO_{0.89}ZnO_{0.1}Ni_{0.01}S$	10 mg / 50 mL	25	180	(Raju et al 2021)
$BiSn_4S_{5.5}$	20 mg / 100 mL	32	10	**Present work**

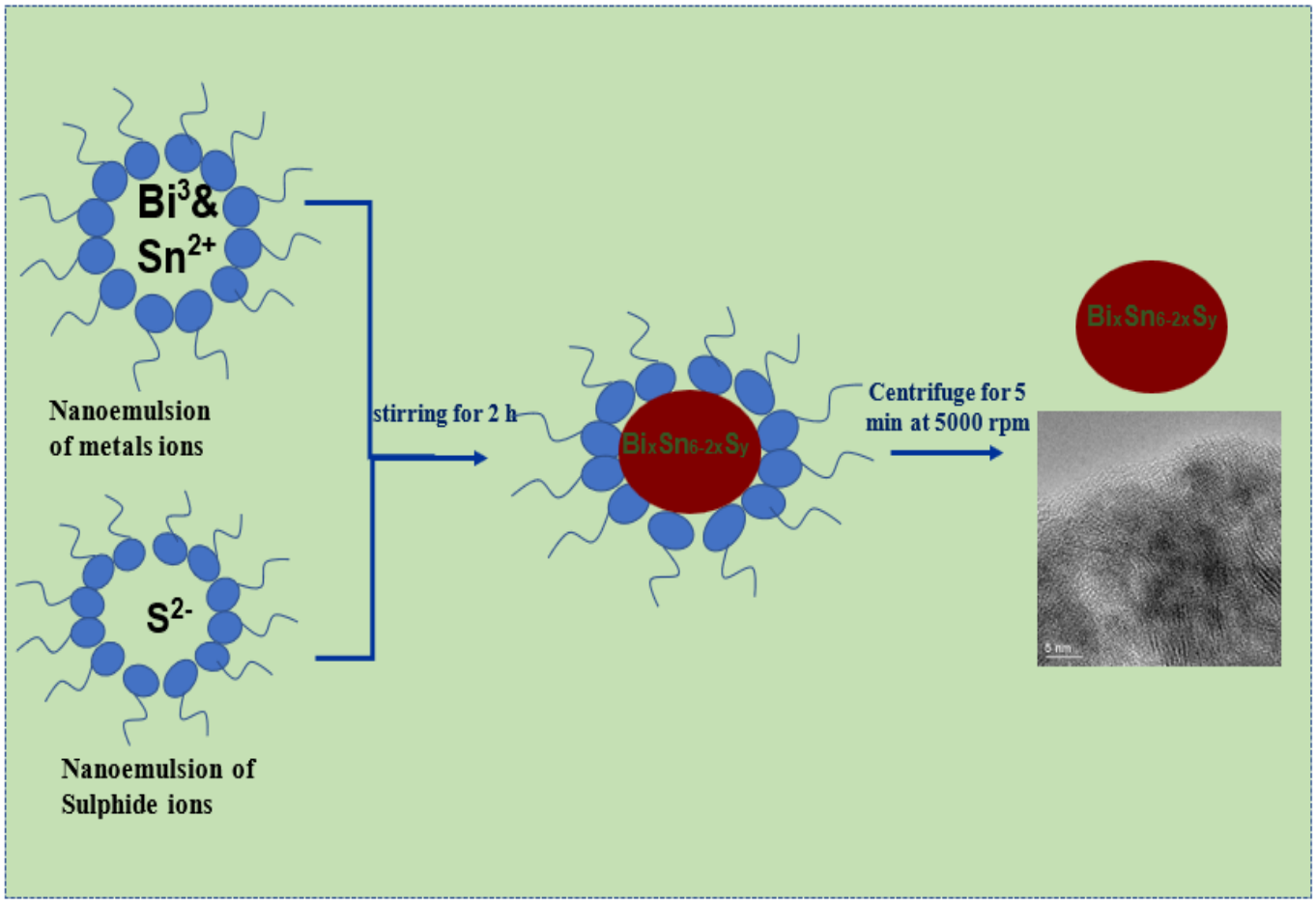

Fig. 1. Graphical representation of the synthesis scheme.

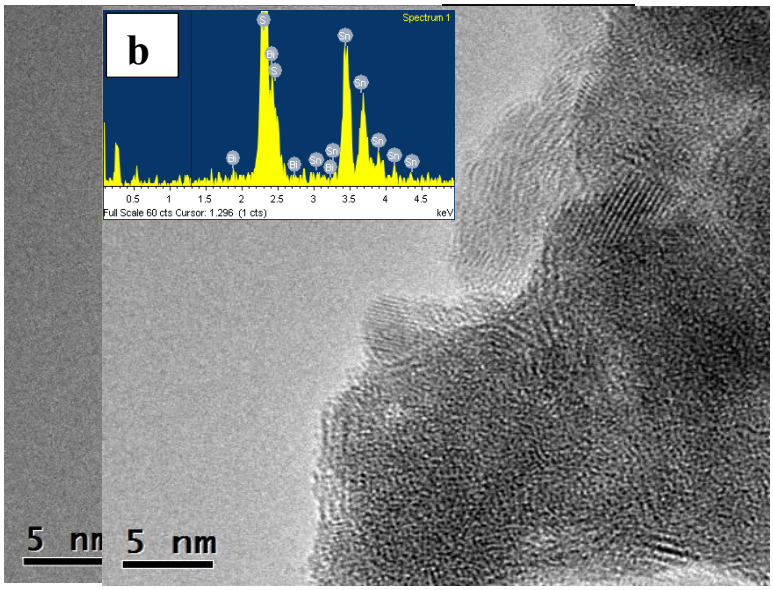

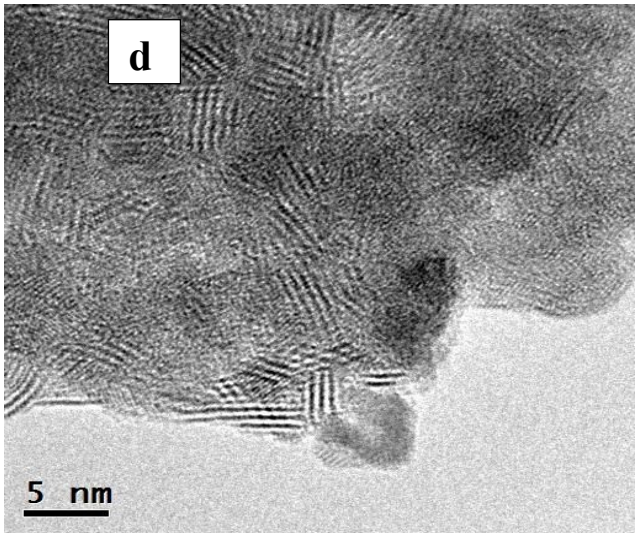

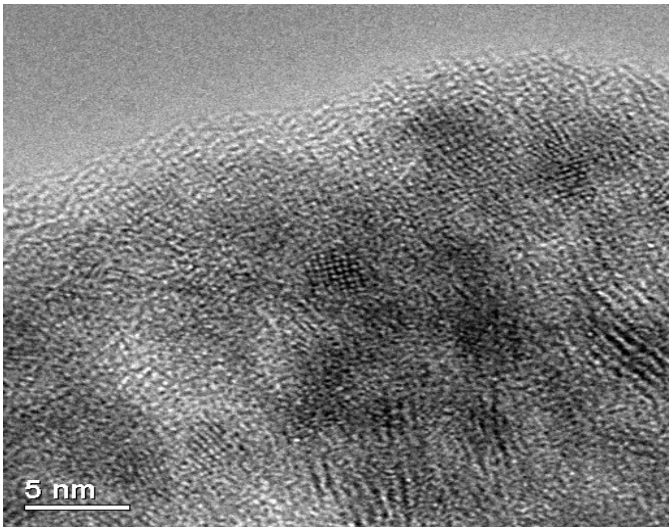

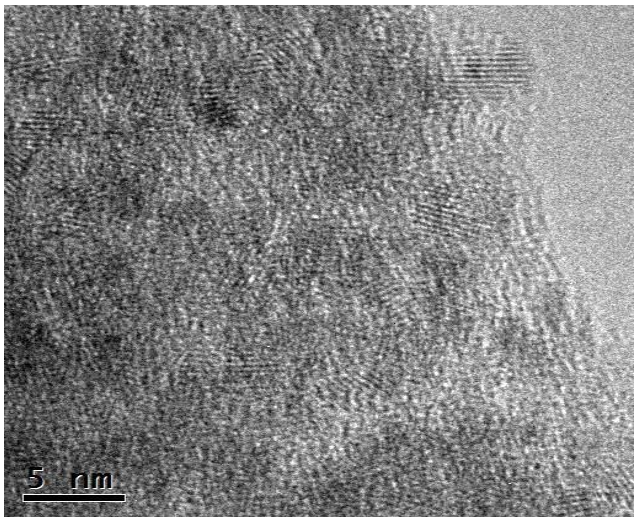

Fig. 2. TEM images of as-synthesized $Bi_xSn_{6-2x}S_y$ nanomaterials: (a) $Bi_{2.95}Sn_{0.1}S_{4.5}$, (b,c) $Bi_{2.14}Sn_{1.71}S_{4.7}$, (d) $BiSn_4S_{5.5}$, and (e) $Bi_{0.3}Sn_{5.34}S_{5.8}$. The inset in (a) displays the fast Fourier transform (FFT) diffraction patterns for the orthorhombic structure of $Bi_{2.95}Sn_{0.1}S_{4.5}$.

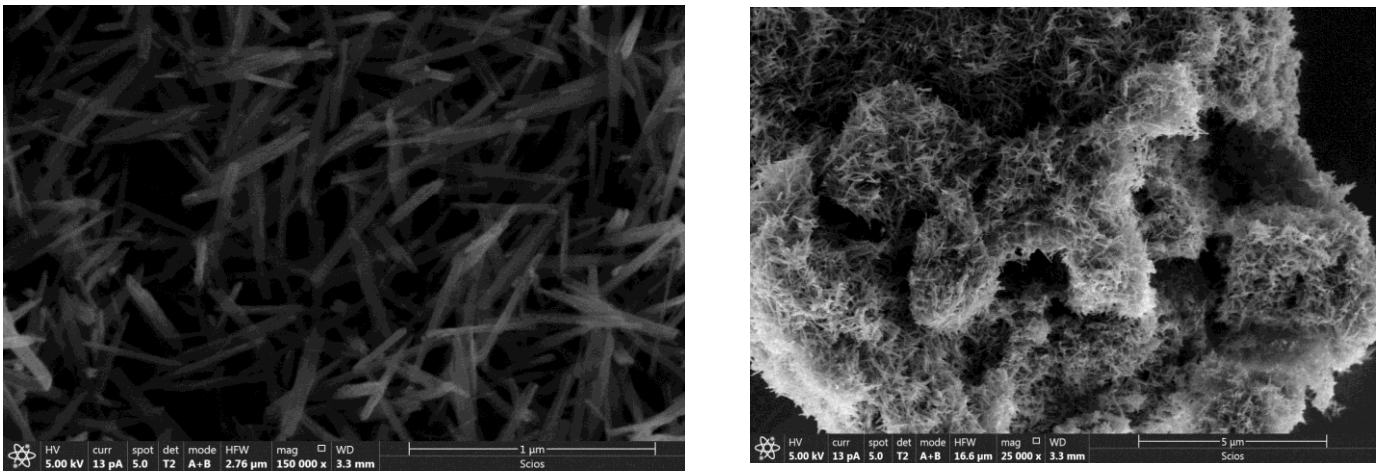

.

Fig. 3. SCIOS images of as-synthesized $Bi_{2.95}Sn_{0.1}S_{4.5}$ with different magnifications.

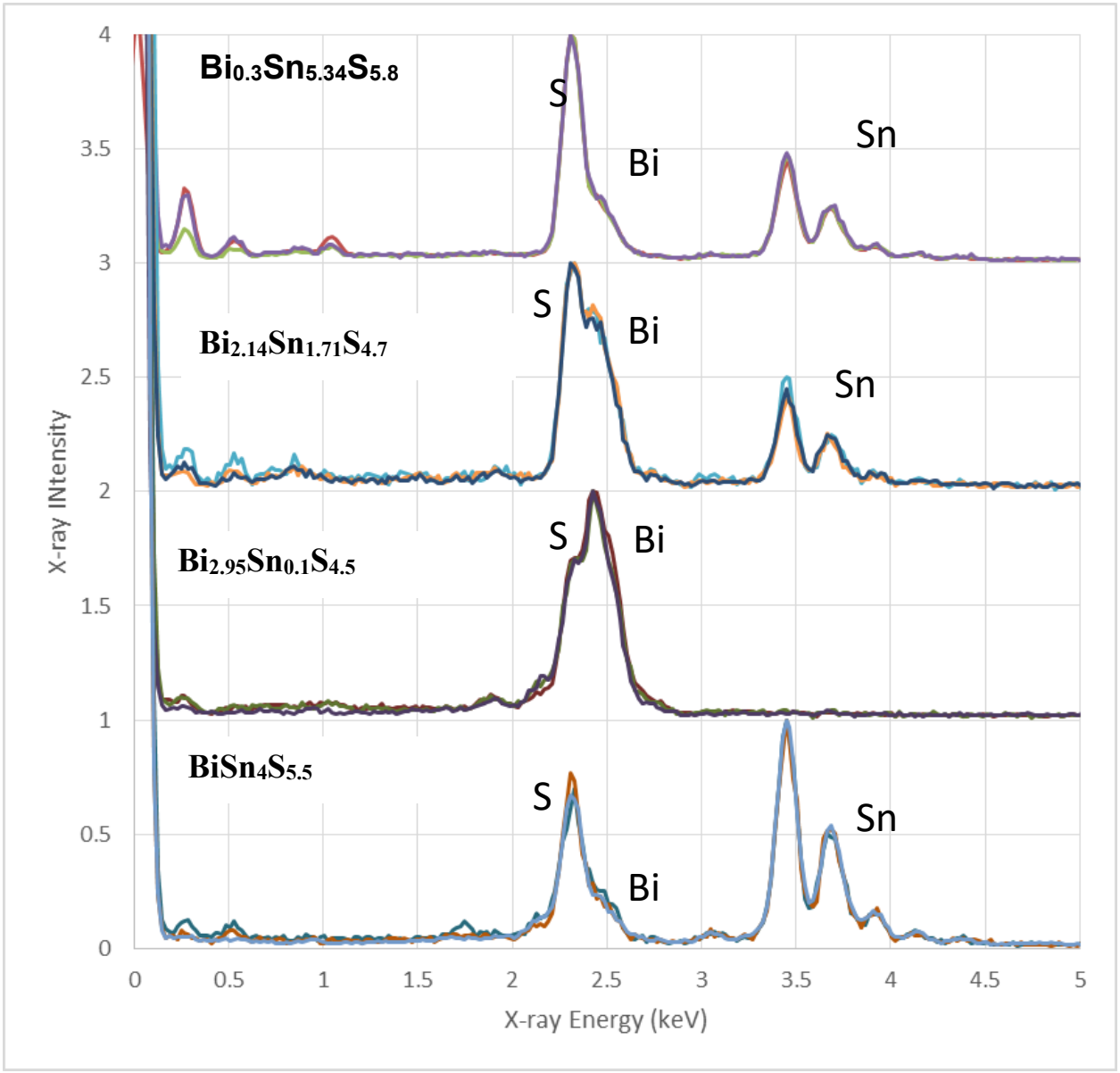

Fig. 4a. EDX spectra of as-synthesized $Bi_xSn_{6-2x}S_y$ nanomaterials.

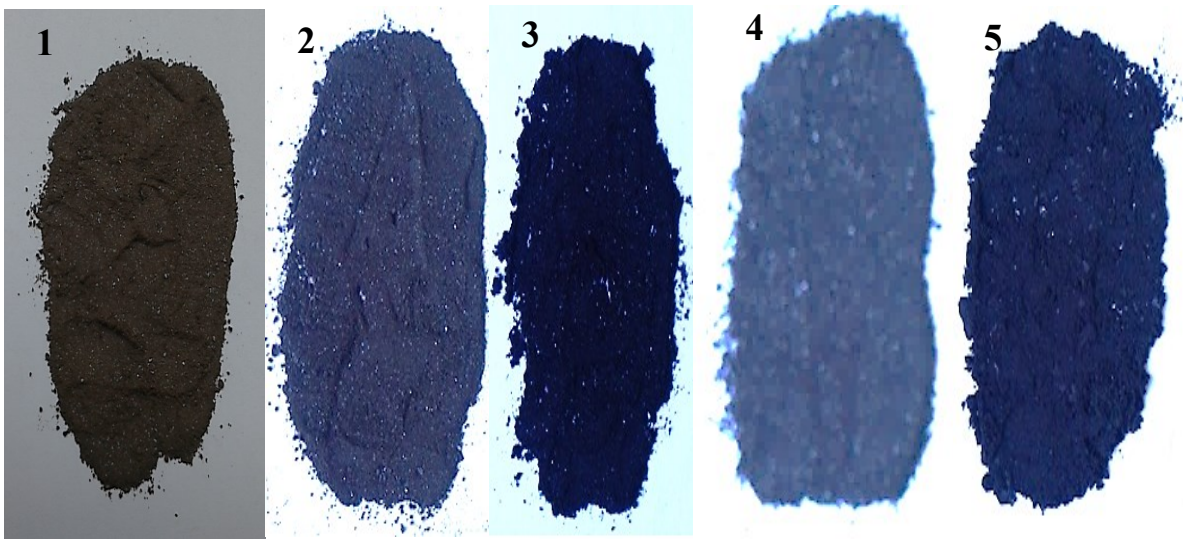

Fig. 4b. Digital image for as-synthesized $Bi_XSn_{6-2X}S_y$; (1) SnS, (2) $Bi_{0.3}Sn_{5.34}S_{5.8}$, (3) $BiSn_4S_{5.5}$, (4) $Bi_{2.14}Sn_{1.71}S_{4.7}$, and (5) $Bi_{2.95}Sn_{0.1}S_{4.5}$ nanomaterials.

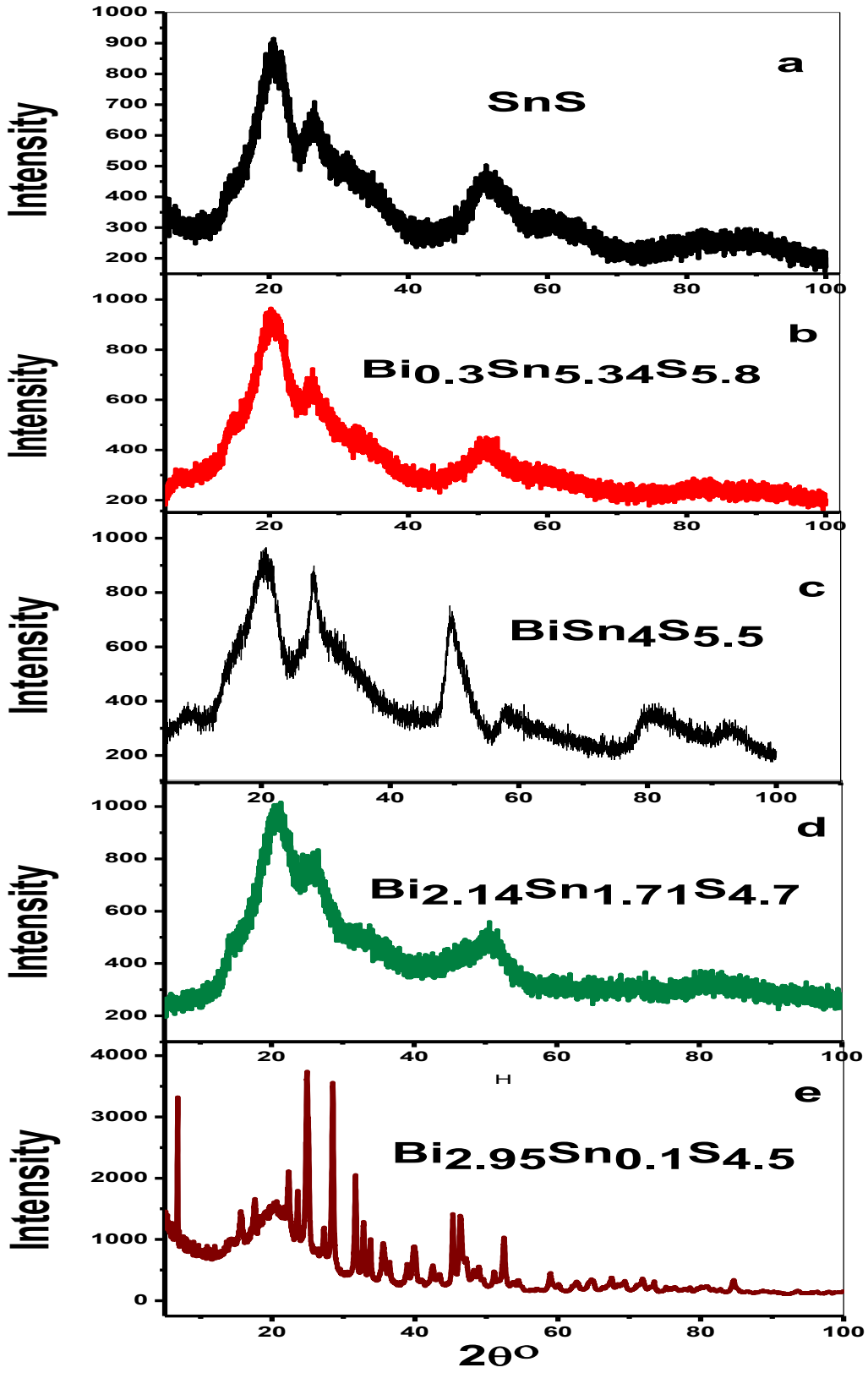

Fig. 5. XRD patterns at room temperature for as-obtained $Bi_XSn_{6-2X}S_y$: (a) SnS, (b) $Bi_{0.3}Sn_{5.34}S_{5.8}$, (c) $BiSn_4S_{5.5}$, (d) $Bi_{2.14}Sn_{1.71}S_{4.7}$, and (e) $Bi_{2.95}Sn_{0.1}S_{4.5}$ nanomaterials.

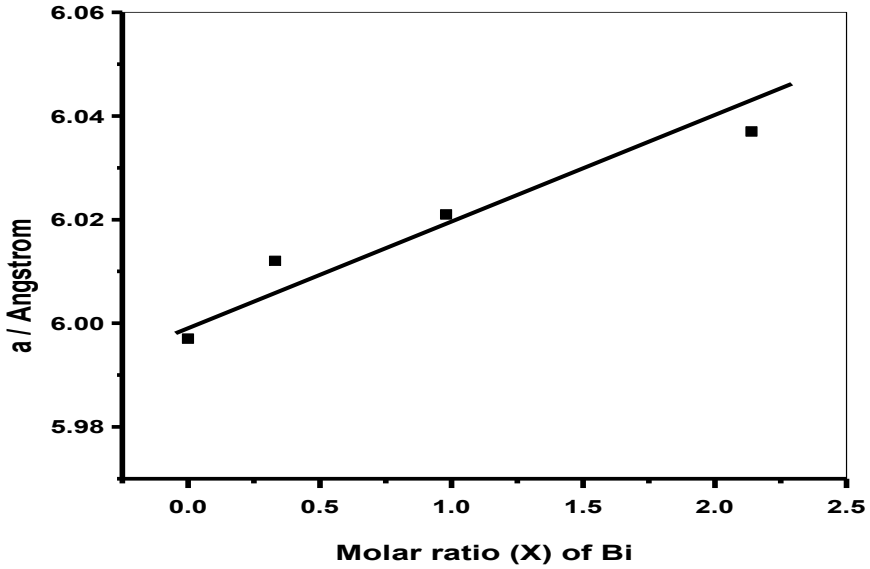

Fig. 6. Obtained parameters of the refined unit cell vs. Bi molar ratio (x).

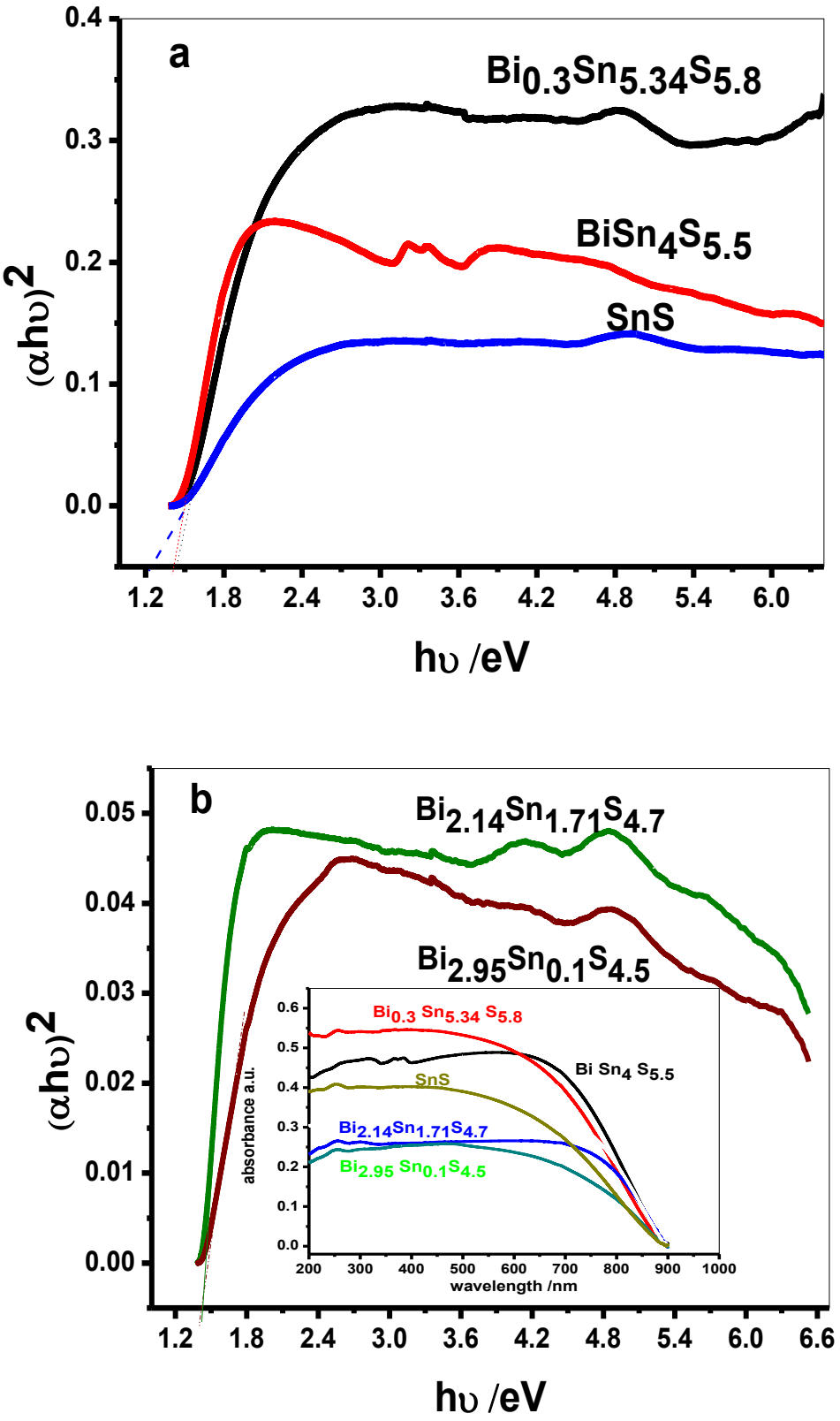

Fig. 7. Kubelka-Munk plots for the absorption of $Bi_xSn_{6-2x}S_y$: (a) SnS, $Bi_{0.3}Sn_{5.34}S_{5.8}$, and $BiSn_4S_{5.5}$, (b) $Bi_{2.14}Sn_{1.71}S_{4.7}$ and $Bi_{2.95}Sn_{0.1}S_{4.5}$. The inset displays UV-visible absorbance spectra (changed from diffuse reflectance spectra) for $Bi_xSn_{6-2x}S_y$.

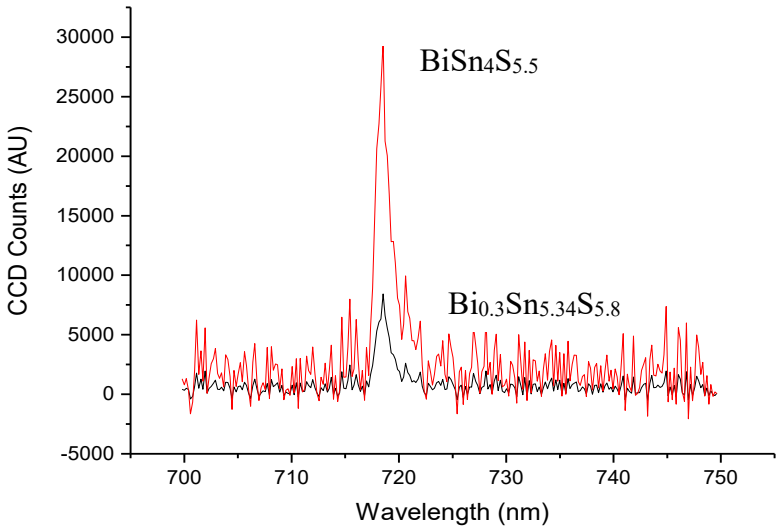

Fig. 8. Photoluminescence (PL) spectra for $BiSn_4S_{5.5}$ and $Bi_{0.3}Sn_{5.34}S_{5.8}$ QDs.

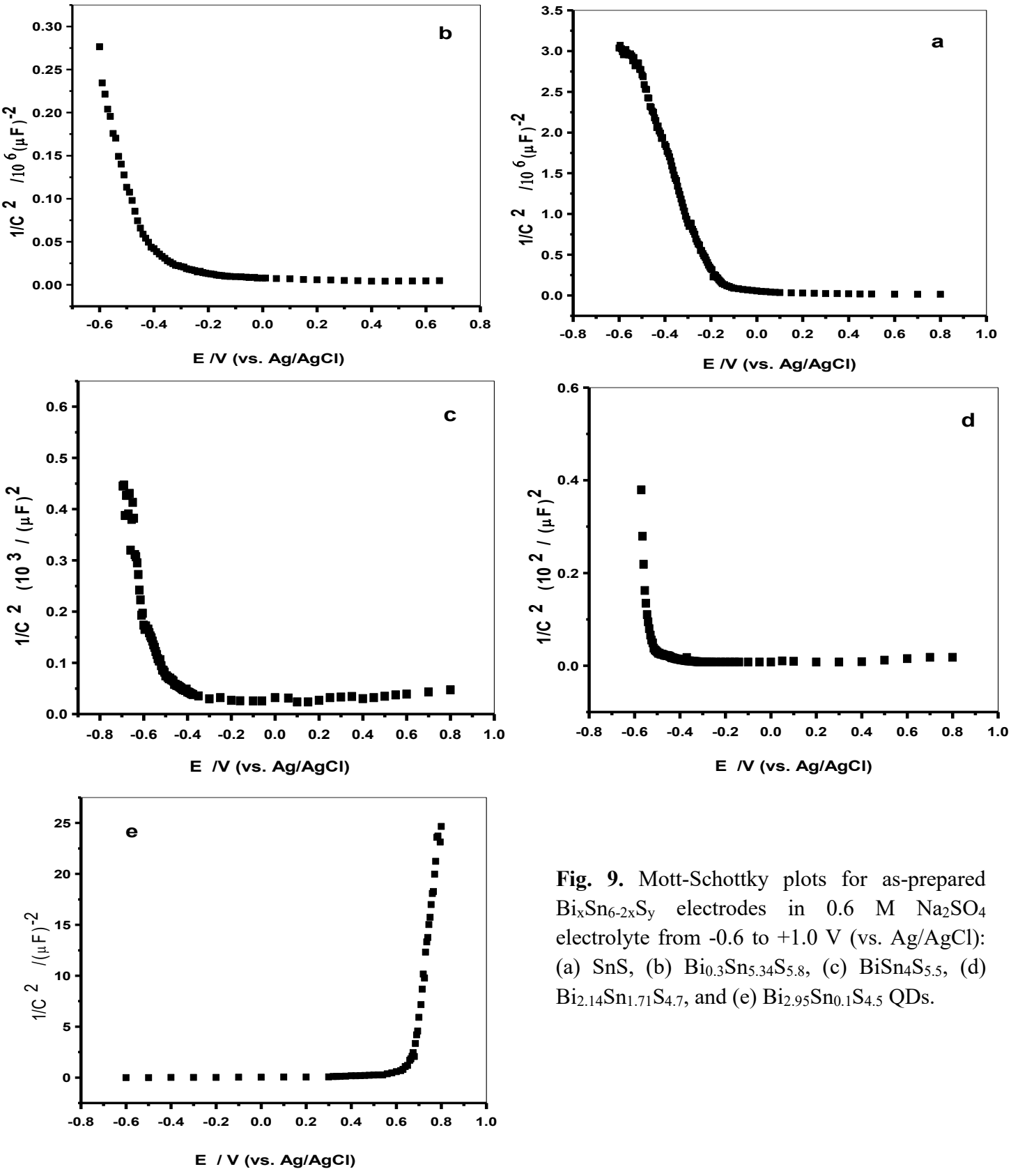

Fig. 9. Mott-Schottky plots for as-prepared $Bi_xSn_{6-2x}S_y$ electrodes in 0.6 M Na_2SO_4 electrolyte from -0.6 to +1.0 V (vs. Ag/AgCl): (a) SnS, (b) $Bi_{0.3}Sn_{5.34}S_{5.8}$, (c) $BiSn_4S_{5.5}$, (d) $Bi_{2.14}Sn_{1.71}S_{4.7}$, and (e) $Bi_{2.95}Sn_{0.1}S_{4.5}$ QDs.

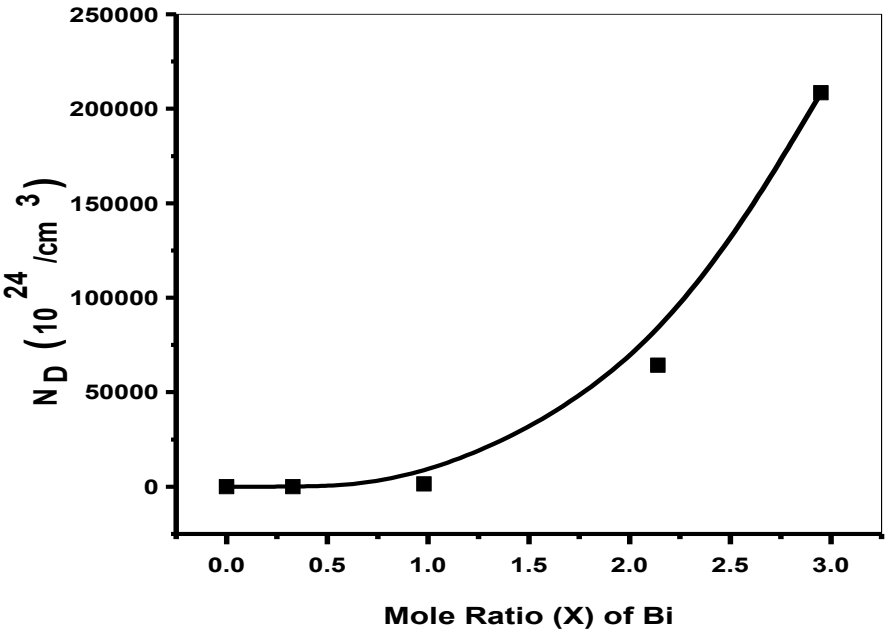

Fig. 10. Charge carrier density (N_D) dependence on the molar ratio (x) of Bi^{3+} for different $Bi_xSn_{6-2x}S_y$ semiconductors QDs.

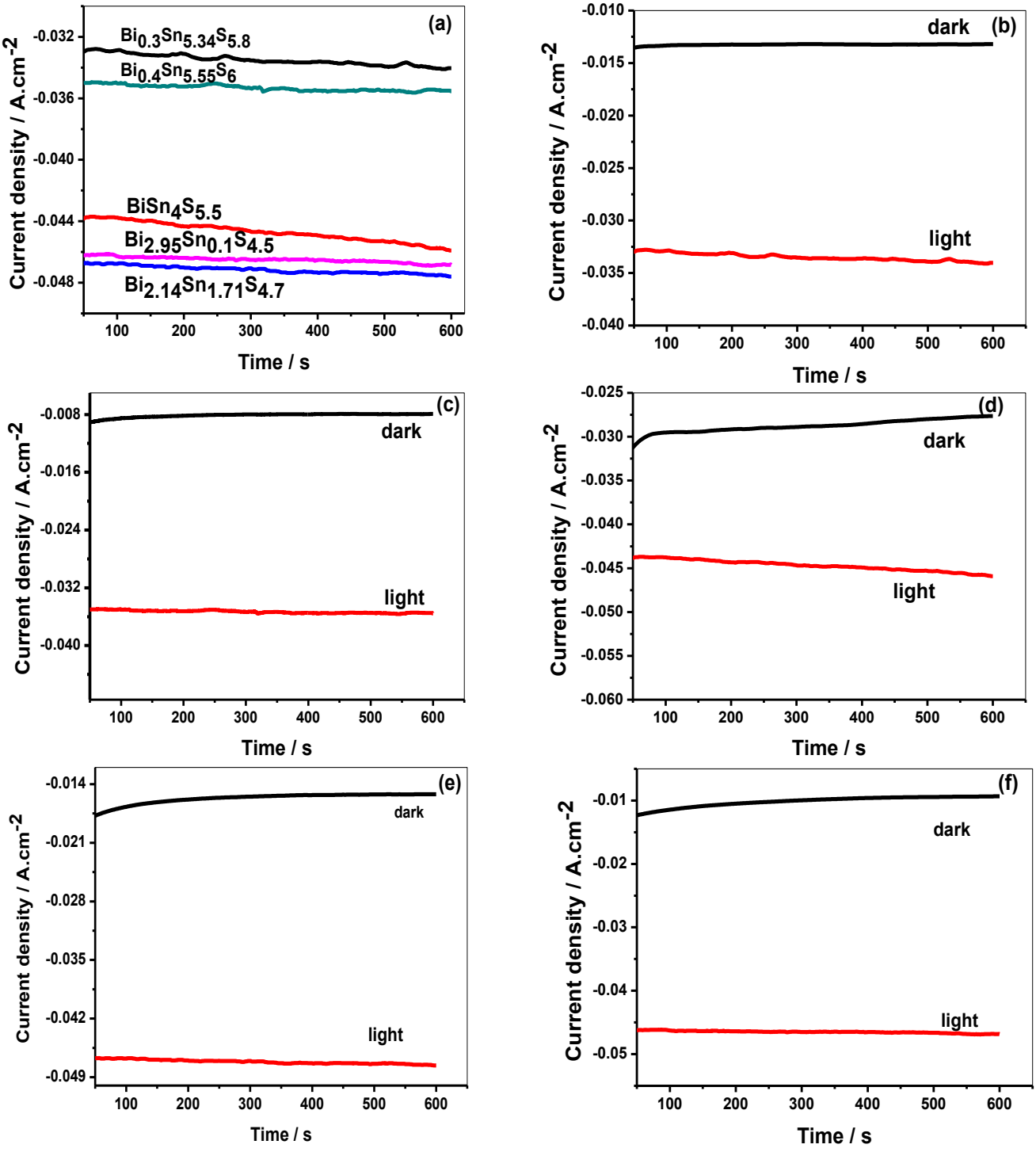

Fig. 11 (a) Photocurrent responses of all BiSnS-prepared electrodes under light conditions. (b) $Bi_{0.3}Sn_{5.34}S_{5.8}$, (c) $Bi_{0.4}Sn_{5.5}S_6$, (d) $BiSn_4S_{5.5}$, (e) $Bi_{2.14}Sn_{1.71}S_{4.7}$, and (f) $Bi_{2.95}Sn_{0.1}S_{4.5}$ photocurrent responses under dark and light conditions. All are measured at an applied potential of 0.65 V (vs. Ag/AgCl) in 0.6 M Na_2SO_4 electrolyte.

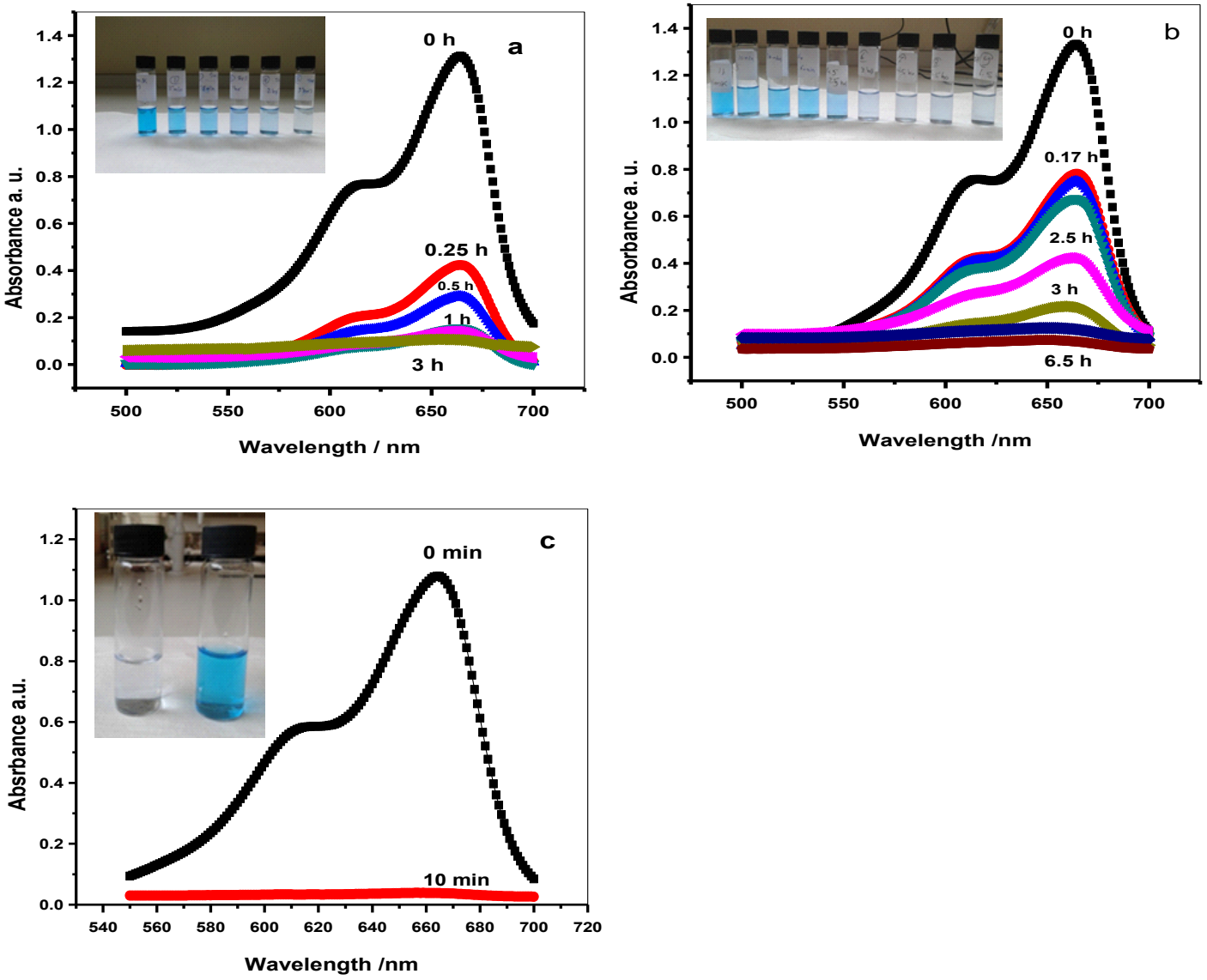

Fig. 12. UV-visible absorption spectra of the MB aqueous solution during the photodegradation under UV-visible irradiation using $Bi_xSn_{6-2x}S_y$: (a) SnS, (b) $Bi_{0.3}Sn_{5.34}S_{5.8}$, and (c) $BiSn_4S_{5.5}$ and containing digital images of the changing color of MB aqueous solutions during its photodegradation.

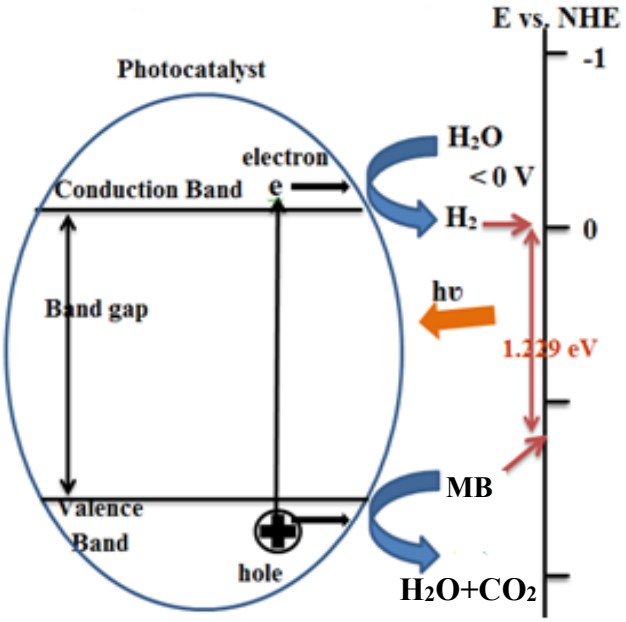

Fig. 13. Schematic mechanism for photodegradation of MB using $Bi_xSn_{6-2x}S_y$ semiconductor QDs.